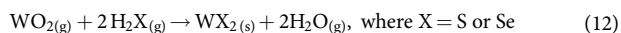


or



Reactions (8)–(10) and (11)–(12) can occur concurrently. The appearance of different molybdenum and tungsten oxidation states can also be directly observed from the colour changes of the solid precursors after exposure to different gaseous environments:  $\text{MoO}_2$  (brown),  $\text{W}_{20}\text{O}_{58}$  (blue), a violet colour indicating the presence of  $\text{W}_{20}\text{O}_{58}$  and  $\text{W}_{18}\text{O}_{49}$  phases in a whisker-type morphology<sup>42</sup> and  $\text{WO}_2$  (chocolate brown) (Extended Data Fig. 5e–l).

There are important differences in the behaviour of molybdenum and tungsten-based compounds in the presence of water vapour<sup>22</sup>. Firstly, the oxide products of tungsten are relatively less volatile than those of the corresponding molybdenum compounds. In addition, the high-index W sub-oxides ( $\text{W}_{20}\text{O}_{58}$ ) are less volatile and less readily oxidized to  $\text{WO}_3$ . This vapour-phase modulation of the oxide species is the key driving force for the observed sequential growth of lateral heterostructures. Thus, the growth mechanism can be summarized as follows. The selective growth of  $\text{MoX}_2$  or  $\text{WX}_2$  monolayers can be achieved simply by controlling the carrier gas environment.  $\text{N}_2 + \text{H}_2\text{O}$  vapour (without  $\text{H}_2$ ) favours the evaporation of both molybdenum and tungsten precursors, but only molybdenum precursors are deposited on the substrate. An abrupt switch of the carrier gas to  $\text{Ar} + \text{H}_2$  quickly depletes the supply of molybdenum precursors, while continuing to supply tungsten precursors owing to the slower reduction rate of  $\text{WO}_x$ . A more detailed chemical analysis, including the type of gaseous by-products, in conjunction with theoretical models is ongoing.

In order to further understand the role of molybdenum or tungsten oxides during the switching of one material domain to the other (such as  $\text{MoX}_2$  to  $\text{WX}_2$ ), and the extent of material diffusion across the interface while changing the carrier gas from  $\text{N}_2 + \text{H}_2\text{O}$  to  $\text{Ar} + \text{H}_2$  for heterostructure fabrication, the oxidation induced evaporation and the rapid reduction behaviour of different solid sources, including  $\text{MoO}_3$  and  $\text{WO}_3$ , were evaluated independently at  $1,060^\circ\text{C}$  (Extended Data Fig. 5c, d).

**Case 1, in the presence of  $\text{H}_2\text{O}$ .** It can be seen from Extended Data Fig. 5c that sublimation of  $\text{MoO}_3$  is almost instantaneous (97% weight loss in 2 min). By contrast, the sublimation of  $\text{WO}_3$  is very slow (approximately 2% weight loss in 2 min) and is linear. This is further supported by the observation that the weight loss of  $\text{MoSe}_2$  is around three times higher than that of  $\text{WSe}_2$  for a 10-min interaction with  $\text{H}_2\text{O}$ , which is otherwise linear. This shows that, in the presence of  $\text{H}_2\text{O}$ , the Mo-oxide vapours dominate over W-oxide vapours in the reaction zone. It can be concluded that, in the presence of water vapour, oxide products of tungsten are relatively less volatile than the corresponding molybdenum compounds. In fact, the slower oxidation of tungsten compounds might aid the formation of tungsten oxide hydroxide ( $\text{WO}_3 \cdot x\text{H}_2\text{O}$ ) species, which generally condense below  $500^\circ\text{C}$ . Hence, an  $\text{H}_2\text{O}$  environment favours the growth of only  $\text{MoX}_2$  domains.

**Case 2, in the presence of  $\text{H}_2$  reducing gas.**  $\text{MoO}_3$  undergoes rapid phase transformation to different sub-oxide phases until it is completely reduced to Mo, via the steps  $\text{MoO}_3 \rightarrow \text{Mo}_4\text{O}_{11} \rightarrow \text{MoO}_2 \rightarrow \text{Mo}$  (Supplementary Table 3)<sup>43</sup>. A weight loss of around 75% was observed in 10 min. In a similar time frame, however,  $\text{WO}_3$  undergoes a linear transformation to different sub-oxide phases via  $\text{WO}_3 \rightarrow \text{W}_n\text{O}_{3n-1} \rightarrow \text{W}_n\text{O}_{3n-2}$  ( $\text{W}_{20}\text{O}_{58}$ )  $\rightarrow \text{W}_{18}\text{O}_{48} \rightarrow \text{WO}_2$  (Supplementary Table 3). A maximum weight loss of 8.5% was observed in 10 min, which is almost 9 times slower than the reduction process of  $\text{MoO}_3$ . It indicates that, during the switching of  $\text{H}_2\text{O}$  to  $\text{H}_2$  carrier gas, the residual  $\text{MoO}_2$  reduces instantaneously; however, the supply of W sub-oxides is maintained. In addition, the leaching of W sub-oxides by  $\text{H}_2$  is more rapid than their rate of reduction to lower W sub-oxides, thus contributing to the growth of the  $\text{WSe}_2$  domain.

From the above observation, it can be concluded that  $\text{H}_2\text{O}$  vapour favours the growth of the  $\text{MoSe}_2$  domain because the population of molybdenum oxides dominates the reaction chamber. The rapid reduction of  $\text{MoO}_3$  indicates (Extended Data Fig. 5d) that the rate of  $\text{MoSe}_2$  oxidation is equal to the rate of  $\text{MoO}_2$  sublimation, meaning that all the  $\text{MoO}_2$  oxide formed during the interaction of  $\text{H}_2\text{O}$  with  $\text{MoSe}_2$  sublimates instantly. This has been further confirmed during the oxidation of  $\text{MoSe}_2$ , in which we do not encounter any signatures of higher Mo-oxide phases. On the other hand,  $\text{H}_2\text{O}$  vapour favours the continuous oxidation of the  $\text{WSe}_2$  precursor to higher sub-oxide phases of W, and the typical timescale of growth of the  $\text{MoSe}_2$  domain does not apply in this case. However, any higher W sub-oxides that occur during  $\text{WSe}_2$  oxidation, such as  $\text{W}_{20}\text{O}_{58}$  or  $\text{WO}_3$ , can effectively capture an  $\text{H}_2\text{O}$  molecule and form tungsten oxide hydroxide ( $\text{WO}_3 \cdot \text{H}_2\text{O}$ ), which is very volatile and hence can only condense below  $500^\circ\text{C}$ . The different interfaces during the transition from one material to other are a consequence of the different oxidation and reduction rates of molybdenum and tungsten-based compounds as well as the gas switching mechanism. When the carrier

gas switches from  $\text{H}_2\text{O}$  to  $\text{H}_2$  (as a reducing agent), the residual Mo-oxide content depletes suddenly, as observed from the weight-loss plot. Because, in the present experimental setup, absolute depletion of  $\text{H}_2\text{O}$  to  $\text{H}_2$  is not possible, this resulted in a mild co-deposition of Mo into the  $\text{WX}_2$  domain, hence forming a smooth interface ( $\text{MoX}_2 \rightarrow \text{WX}_2$ ). Note that, during the continuous growth of the  $\text{WX}_2$  domain, the Mo-oxide completely depletes into metallic molybdenum over the  $\text{MoX}_2$  source. When the condition is reverted—that is, changing from  $\text{H}_2$  to  $\text{H}_2\text{O}$  vapour—the W sub-oxides proceed towards forming high-index W sub-oxides, as indicated by the slow weight-loss of W-oxide precursors in  $\text{H}_2\text{O}$ . Meanwhile,  $\text{H}_2\text{O}$  restores the initial oxidation step from metallic molybdenum that, during the interaction with  $\text{H}_2$  gas, formed at the  $\text{MoX}_2$  surface. This forms  $\text{MoO}_2$  relatively more slowly than the direct oxidation of the  $\text{MoX}_2$  source. This might result in a slight delay to the supply of  $\text{MoO}_2$  vapour to the already existing  $\text{WX}_2$  edge-site, and hence always results in a sharp transition from the  $\text{WX}_2$  to the  $\text{MoX}_2$  domain.

**Assignment of Raman modes of  $\text{MoSe}_{0.64}\text{Se}_{1.36}$ – $\text{WSe}_{1.32}\text{S}_{0.68}$  lateral heterostructure.** The compositional and spatial distribution of (S–Se) alloy in the  $\text{MoSe}_{2(1-x)}\text{Se}_{2x}$ – $\text{WS}_{2(1-x)}\text{Se}_{2x}$  lateral heterostructures were examined using Raman measurements (Fig. 3a, b and Extended Data Figs 8, 10). The normalized Raman spectra in Extended Data Fig. 8c indicate that the  $\text{MoX}_2$ - and  $\text{WX}_2$ -related Raman branches are well separated, and mostly consist of several intense peaks in the range of  $100$  to  $500\text{ cm}^{-1}$ . The intense Raman peaks (Extended Data Fig. 8c) observed within domains 1 and 3 (Extended Data Fig. 8a) are related to an alloy phase of  $\text{MoSe}_{2(1-x)}\text{Se}_{2x}$  (refs 28, 44). In general,  $\text{A}_{1g}$  and  $\text{E}_{2g}$  modes in monolayer  $\text{MoSe}_{2(1-x)}\text{Se}_{2x}$  show typical two-mode behaviour and do not imply phase segregation<sup>44</sup>. Splitting of the  $\text{A}_{1g}$  mode has also been observed, which is attributed mainly to the mass difference between Se and S as well as their spatial configuration around Mo atoms<sup>44</sup>. Hence, the observed Raman spectra (Extended Data Fig. 8c) for the  $\text{MoSe}_{2(1-x)}\text{Se}_{2x}$  monolayer domains have two distinct sets of features:  $\text{MoSe}_2$ -like features ( $\text{E}_{2g}(\text{S–Mo})$  ( $370\text{ cm}^{-1}$ ) and  $\text{A}_{1g}(\text{S–Mo})$  ( $400.5\text{ cm}^{-1}$ )), and  $\text{MoSe}_2$ -like features close to  $264\text{ cm}^{-1}$ . In detail, the peaks at  $219\text{ cm}^{-1}$  and  $264\text{ cm}^{-1}$  are observed as a result of  $\text{A}_{1g}$  mode splitting of the  $\text{MoSe}_2$  phase into low and high-frequency domains, respectively, whereas  $\text{MoSe}_2$ -like  $\text{A}_{1g}$  shifts from  $405$  to  $400.5\text{ cm}^{-1}$ , and  $\text{E}_{2g}$  shifts from  $385$  to  $370\text{ cm}^{-1}$ , confirm the presence of Se incorporation in the lattice site of S (ref. 45). Similarly, the normalized Raman spectra corresponding to domains 2 and 4 (Extended Data Fig. 8a) display several phonon modes typical of a  $\text{WSe}_{2x}\text{S}_{2(1-x)}$  alloy, which can be assigned to modes  $\text{A}_{1g}(\text{Se–W})$  ( $256$ – $259\text{ cm}^{-1}$ ),  $\text{A}_{1g}(\text{S–W})$  ( $404$ – $406\text{ cm}^{-1}$ ),  $\text{A}_{1g}(\text{S–W–Se})$  ( $379$ – $381\text{ cm}^{-1}$ ),  $\text{E}_{2g}(\text{S–W})$  ( $354\text{ cm}^{-1}$ ),  $\text{A}_{1g}(\text{m})$ – $\text{LA}_{1g}(\text{S–W})$  ( $225\text{ cm}^{-1}$ ) and  $\text{A}_{1g}(\text{Se–W})$ – $\text{LA}_{1g}(\text{S–W})$  ( $138$ – $141\text{ cm}^{-1}$ ) (ref. 27). The observed red shift (around  $12\text{ cm}^{-1}$ ) of the  $\text{A}_{1g}(\text{S–W})$  mode in a Se-rich environment, as compared to that of isotropic monolayer  $\text{WS}_2$  phase and the corresponding hardening of the  $\text{A}_{1g}(\text{Se–W})$  mode, clearly indicates the presence of Se/S alloy in  $\text{MoSe}_{2(1-x)}\text{Se}_{2x}$  and  $\text{WS}_{2(1-x)}\text{Se}_{2x}$  domains. However, the position of the  $\text{E}_{2g}(\text{S–W})$  mode does not change ( $\pm 1\text{ cm}^{-1}$ ), which might be attributed to the weak coupling between the very weak  $\text{E}_{2g}(\text{Se–W})$  mode and the strong  $\text{E}_{2g}(\text{S–W})$  mode<sup>27</sup>. This has been further confirmed by Raman intensity mapping as shown in the composite image (individual component maps in Extended Data Fig. 8h–k). Even though the  $\text{A}_{1g}(\text{S–W})$  and  $\text{A}_{1g}(\text{S–Mo})$  peaks differ by only around  $4\text{ cm}^{-1}$ , the mapping provides clear in-plane differentiation between these two domains that matches the optical contrast of the heterostructure.

**Assignment of Raman modes of  $\text{MoSe}_{0.96}\text{S}_{1.04}$ – $\text{WSe}_{0.92}\text{S}_{1.08}$  lateral heterostructure.** Extended Data Fig. 10b shows the  $\text{MoSe}_{2(1-x)}\text{S}_{2x}$  and  $\text{WS}_{2(1-x)}\text{Se}_{2x}$  related Raman spectra at different regions of the heterostructure (including the junctions) corresponding to the optical image in Fig. 3b. The prominent peaks, observed within domain 1 and 3 (Extended Data Fig. 10a), are mostly related to an alloy phase of  $\text{MoSe}_{2(1-x)}\text{S}_{2x}$ , which can be assigned to  $\text{MoSe}_2$ -like peaks ( $\text{A}_{1g}(\text{S–Mo})$  modes ( $402.5\text{ cm}^{-1}$ ),  $\text{E}_{2g}(\text{S–Mo})$  ( $371$ – $374\text{ cm}^{-1}$ )) and  $\text{MoSe}_2$ -like peaks (high frequency  $\text{A}_{1g}(\text{Se–Mo})$  modes ( $266$ – $267\text{ cm}^{-1}$ ), low frequency  $\text{A}_{1g}(\text{Se–Mo})$  modes ( $223\text{ cm}^{-1}$ ), and  $\text{E}_{2g}(\text{Se–Mo})$  ( $277$ – $278\text{ cm}^{-1}$ )). Similarly, Raman spectra collected from domains 2 and 4 display several modes that correspond to a typical  $\text{WS}_{2(1-x)}\text{Se}_{2x}$  alloy, and can be assigned to modes  $\text{A}_{1g}(\text{S–W})$  ( $211$ – $213\text{ cm}^{-1}$ ),  $\text{A}_{1g}(\text{Se–W})$  ( $263\text{ cm}^{-1}$ ),  $\text{E}_{2g}(\text{S–W})$  (around  $356$ – $358\text{ cm}^{-1}$ ),  $\text{A}_{1g}(\text{m})$ – $\text{LA}_{1g}(\text{S–W})$  (around  $225\text{ cm}^{-1}$ ) and  $\text{A}_{1g}(\text{Se–W})$ – $\text{LA}_{1g}(\text{S–W})$  +  $\text{E}_{2g}(\text{S–W})$ – $\text{LA}_{1g}(\text{S–W})$  (around  $160\text{ cm}^{-1}$ ). The  $\text{A}_{1g}(\text{S–W})$  mode is red shifted by approximately  $4\text{ cm}^{-1}$ , whereas the corresponding large shift of the  $\text{A}_{1g}(\text{Se–W})$  mode is due to the occurrence of uniform S/Se alloying in these heterostructures. This is supported by the distinct photoluminescence spectra (Extended Data Fig. 10c, d) collected from the  $\text{MoSe}_{2(1-x)}\text{S}_{2x}$  and  $\text{WS}_{2(1-x)}\text{Se}_{2x}$  domains. The individual Raman and photoluminescence maps further confirm the seamless connectivity as well as uniformity in the distribution of S/Se alloy within the triangular domains (Extended Data Fig. 10).

**Data availability.** The datasets generated and/or analysed in the current study are available from the corresponding authors upon reasonable request, and are also included with the manuscript as Extended Data and Supplementary Information.